MitoXRNet: Deep Learning-enabled 3D Segmentation of Mitochondria and Nucleus in Soft X-ray Tomograms

Arun Yadav[1], Aneesh Deshmukh[2], Pushkar Bharadwaj[3], Anuj Baliyan[4], Kate White[2,5], Jitin Singla[1,6,7]

[1] Department of Computer Science and Engineering, Indian Institute of Technology (IIT) Roorkee, Roorkee, Uttarakhand, India
[2] Department of Chemistry, Bridge Institute, Michelson Center for Convergent Bioscience, University of Southern California, Los Angeles, CA, USA
[3] Department of Earthquake Engineering, Indian Institute of Technology (IIT) Roorkee, Roorkee, Uttarakhand, India
[4] Department of Electronics and Communication Engineering, Indian Institute of Technology (IIT) Roorkee, Roorkee, Uttarakhand, India
[5] Department of Quantitative Computational Biology, University of Southern California, Los Angeles, CA, USA
[6] Department of Biosciences and Bioengineering, Indian Institute of Technology (IIT) Roorkee, Roorkee, Uttarakhand, India
[7] Lead Contant

Abstract

Mitochondrial morphology and distribution are central to cellular function, but large-scale quantification is limited by the lack of efficient segmentation tools. Soft X-ray tomography (SXT) enables whole-cell, high-resolution imaging of cells in their native state, but segmentation of organelles remains a major bottleneck. We present MitoXRNet, an automated 3D segmentation method for mitochondria and the nucleus in SXT tomograms. The training data were generated by slicing tomograms into overlapping 3D volumes along all three axes, and a Sobel-based preprocessing step enhancing mitochondrial boundaries. MitoXRNet was trained using Binary Cross-Entropy or a combined BCE with Robust Dice loss to address class imbalance. On INS-1E cell line datasets, a compact model (1.4M parameters) outperformed prior 2D U-Nets and the self-configuring nnU-Net (31.2M) with a Dice score of 73.8%. A larger variant (22.6M) achieved strong generalization across unseen datasets. MitoXRNet enables scalable, accurate, and high-throughput segmentation for systematic studies of mitochondrial morphology and cellular architecture.

Subject areas

Mitochondria Segmentation, Deep Learning, Soft X-Ray Tomography

Introduction

Inter-organelle interactions, organelle distribution, shape and size play a vital role in normal cellular function. Quantifying the structural organization of organelles has been challenging due to the range of scales encountered in cell biology and the limitations of traditional imaging approaches, like fluorescent imaging, which require probe tagging — disturbing the native state of the cell. Among available imaging techniques, Soft X-ray Tomography (SXT) can capture the high-resolution images of the whole 3D

cells in their native state (without staining) and within a span of 5 min[1–3]. SXT provides an opportunity to study cells at ultrastructural (mesoscale) scale. It allows us to study cellular organelles, their morphology and spatial alignment within the cell[4–6]. The systematic study of mitochondrial morphology, temporal dynamics and the effect of drug treatments require binary masks of mitochondria segmented out from noisy grayscale 3D SXT tomograms. Most of the analysis currently available in the literature has been conducted on manually segmented masks. Manual segmentation is a time consuming and error prone process. It is also prone to human variability. An expert can take up to 2 days to manually segment complete mitochondrial network per tomogram. This drastically limits the potential of SXT for quantifying morphological changes which require hundreds of segmented cells.

Deep Learning (DL) based segmentation can play an important role in providing efficient solutions for segmenting cellular organelles from tomograms. Although a substantial amount of literature has been published around cell and mitochondria segmentation using various imaging modalities, such as fluorescent microscopy[7–11] and electron microscopy[12–16], etc., limited studies are available for Soft X-ray Tomography[17–22]. Electron microscopy generates high resolution images and has sharp organelle boundaries, whereas SXT tomograms have low contrast, making it challenging to segment cellular structures. On other hand, fluorescence images do not require manual segmentation, as the ground truth can be generated by thresholding the fluorescent labels, with little to no human error. Also, collecting large amounts of training data is relatively more feasible. Additionally, models like nnU-Net[23] self-configures U-Net architecture, loss functions and preprocessing techniques based on input data, making them invariant to imaging techniques. It has been shown to work well on large number of biomedical imaging data for segmentation.

DL-models around soft X-ray tomography are comparatively less explored. Firstly, because the contrast overlap between organelles makes it challenging, secondly, limited manually labelled data is available. Francis et al.[17] proposed a CNN-based method to apply partially labeled data for full label segmentation and showed that mixed labels (partially and fully annotated) perform better than standard fully annotated data-based training[24]. Authors achieved 57.5% dice score on the mitochondrial network. Further, Li et al.[18], published a method wherein they trained 2D U-Net architecture on slices of the tomograms for segmenting cytoplasm, nucleus, mitochondria and vesicles. Using 2D slices from all three-axis generated ample amount of training data from the limited 3D annotated data. For mitochondrial segmentation they achieved a dice score of 68.34% on three in-domain test cells. Two more studies focusing solely on cytoplasm[19] (ACSeg) and nucleus[20] segmentation have also been recently published.

We hypothesize that organelle segmentation requires 3D context and that 2D slices may not preserve the full context of organelles and subcellar structures. A model can

easily confuse the circular cross-section of mitochondria and vesicle without any volumetric context.

In this paper we propose MitoXRNet: a 3D U-Net based auto-segmentation technique to segment mitochondria from SXT tomograms. The proposed method uses overlapping 3D slices of the whole tomogram along the three axes for generating large training data from limited annotated dataset. We applied a Sobel filter–based custom preprocessing pipeline to highlight the mitochondria boundary. We trained and tested the model with two loss functions: the conventional Binary Cross-Entropy (BCE) loss and a combined BCE with Robust Dice loss. BCE focuses on voxel-level accuracy, while the Robust Dice component improves the overall overlap between predictions and ground truth. In addition, Robust Dice effectively handles class imbalance, which is critical in our case since the mitochondrial volume is substantially smaller than the cell volume.

We trained and tested our method on the same INS-1E (pancreatic β-cell line) SXT dataset as done by Li et al.[18], along with additional cells in the training data set. We also used another independent dataset treated with various drugs, collected from the same source but with different set of microscope calibration and settings (better zone plate resolution). This separate dataset was used to measure out-of-domain performance of the models.

We trained models with two different depths and varying kernel filters:

i. A smaller model with only 1.4 million (M) parameters outperformed Li et al.[18] results and state-of-the-art models like nnU-Net[23](auto configured with 31.2M parameters) on the in-domain test dataset. The smaller model could not generalize well compared to nnU-Net on out-of-domain dataset.
ii. A larger model with 22.6M parameters that showed similar performance on in-domain dataset and outperformed nnU-Net on out-domain test dataset.

MitoXRNet results showed improved mitochondrial segmentation with adequate preprocessing and proposed 3D slicing. We also segmented nucleus along with mitochondria, as it provides a basis for analyzing the distribution of mitochondria in the cytosol of the cell. With the increasing availability of SXT[25] and its use in studying cellular architecture and morphological changes under various stress and disease conditions, the requirement for auto-segmentation tools will only increase. SXT is also a growing imaging modality with potential to contribute to whole-cell modeling efforts[26–29]. Our method can help researchers segment hundreds of tomograms with much higher efficiency and study architectural changes to mitochondria using soft X-Ray tomography.

Results

Auto-segmentation workflow

A single SXT tomogram contains whole 3D cell(s) inside a glass capillary, typically oriented vertically. To develop an accurate segmentation of mitochondria and nucleus, first single cells were segmented out using ACSeg[19], available on Biomedisa. The cell masks obtained from ACSeg were manually corrected to limit the error propagation in the downstream training process. The rest of the workflow uses tomograms masked with the ACSeg obtained cell masks, i.e. single cell per tomogram. Figure 1 illustrates the complete workflow of our proposed method. Once the tomograms were masked to get single cells, we performed Sobel-based high pass filter preprocessing and resizing (Methods: Resizing and 3D Slicing). Next, the tomograms along with ground truth masks for the nucleus and mitochondria were sliced into 3D 64-voxel thick slices along all three axes. The 3D slices had an overlap of 32 voxels along the thickness. This generated a total of 63 3D slices from each tomogram (Figure 1A). The 3D U-Net model was trained (Methods: Model training) using either BCE loss or a combination of BCE and Robust Dice loss (Figure 1B). The details of the loss function and other architectural parameters for the model are mentioned in the Methods: Loss functions. For prediction on a new cell, the cell was similarly divided into 3D slices, and the probabilistic predictions were merged into a single complete mask by averaging the probability values for each voxel independently (Figure 1C, Methods: Merge 3D slice predictions).

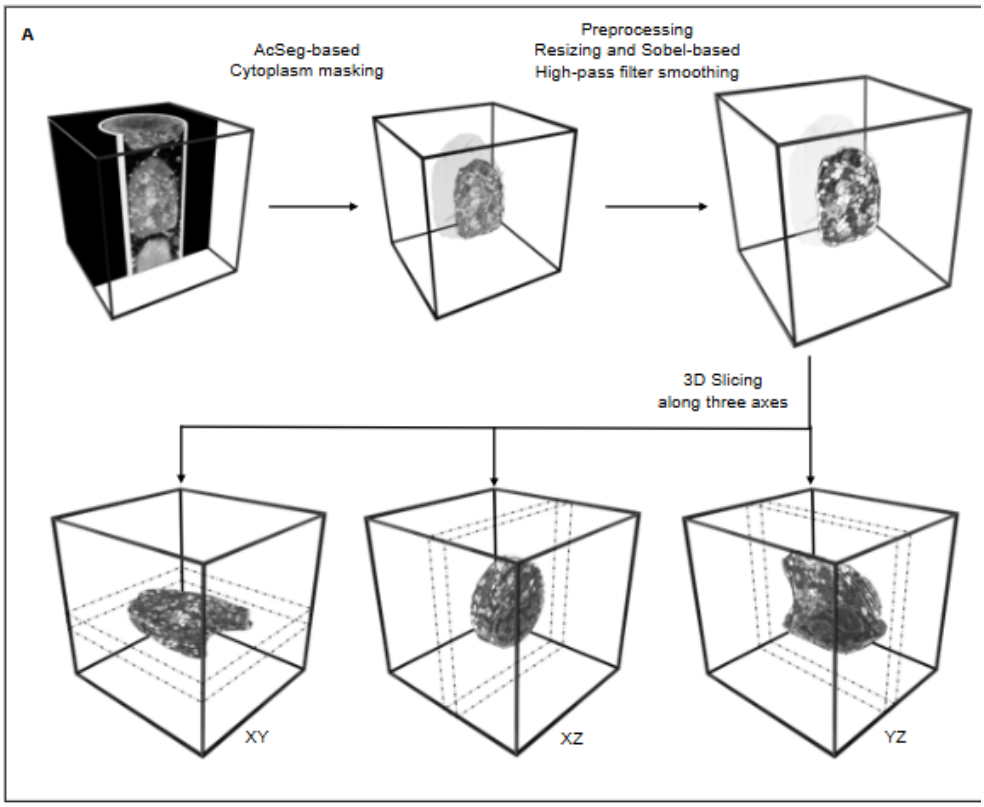

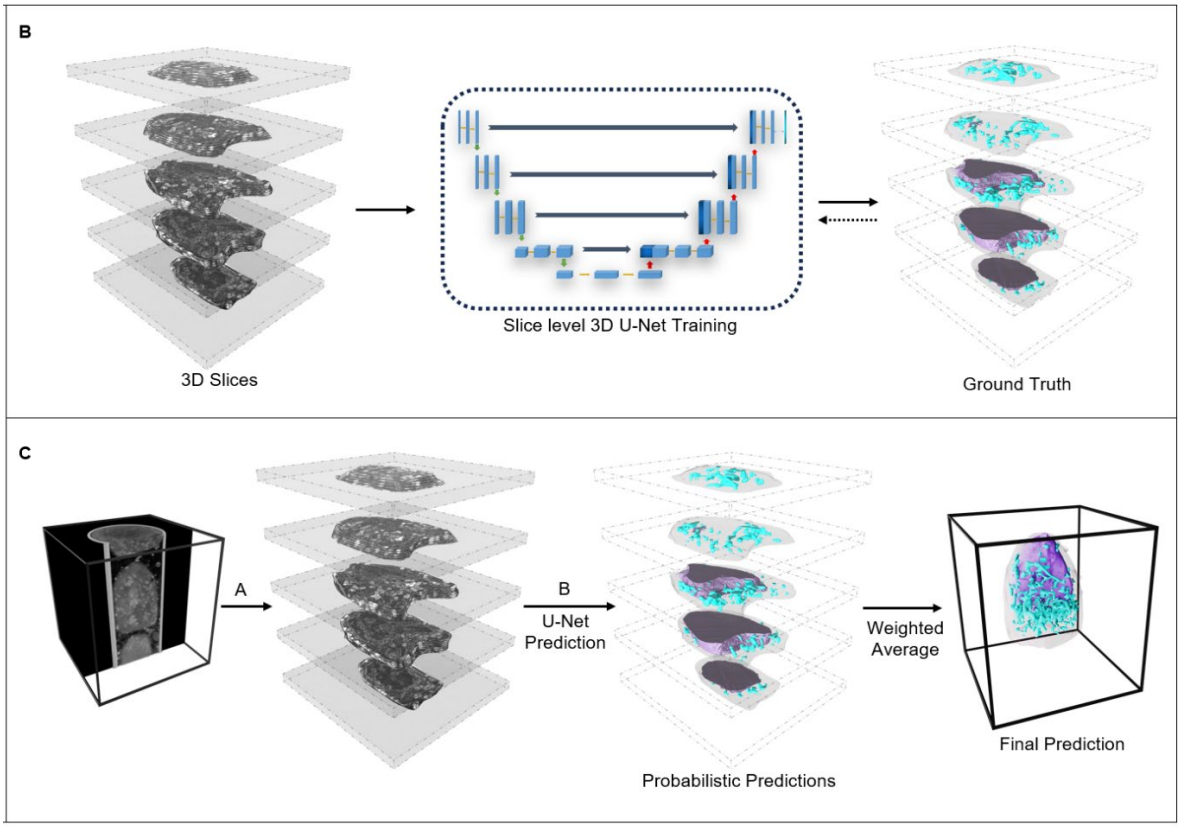

Figure 1: Auto-segmentation workflow for mitochondria and nucleus

(A) 3D slicing: Workflow showing the cell masking using ACSeg, Preprocessing and Resizing, and 3D slicing along the three axes.

(B) Training: 3D slices of tomogram and ground truth are used for training the 3D U-Net model.

(C) Testing: Test tomogram is sliced into 3D slices as shown in (A), mitochondria and nucleus masks are predicted using the model trained in (B), and finally, all the predicted masks are merged to generate final whole-cell mitochondria and nucleus masks.

Preprocessing

The detection of mitochondria in raw SXT tomograms can be challenging, firstly, due to overlaps in intensity values of different organelle regions (Figure 2A) and secondly, mitochondria exhibit very complex, tubular, dynamic architecture with varying widths, lengths and shapes (Figure 2B). Therefore, preprocessing methods that can highlight mitochondria and enhance their boundary are essential for auto-detection and segmentation. The nucleus on the other hand, can easily be detected due to much simpler surface morphology.

There are numerous techniques to enhance the contrast and edges of objects in the images[30–33]. MitoXRNet utilizes nonlinear Sobel-based high-pass enhancement with Gaussian smoothing and normalization enhancing the boundary of the mitochondria in the tomogram. Detailed methodology is provided in the Methods section (Preprocessing of 3D Soft X-Ray tomograms). Figure 2C shows ortho slices of the tomogram processed with Adaptive Histogram Equalization (AHE) as compared to our proposed Sobel-based high-pass filter. The mitochondrial boundaries are significantly

enhanced and much more easily detectable with our proposed filter. We thus used this preprocessing technique for further downstream training and testing.

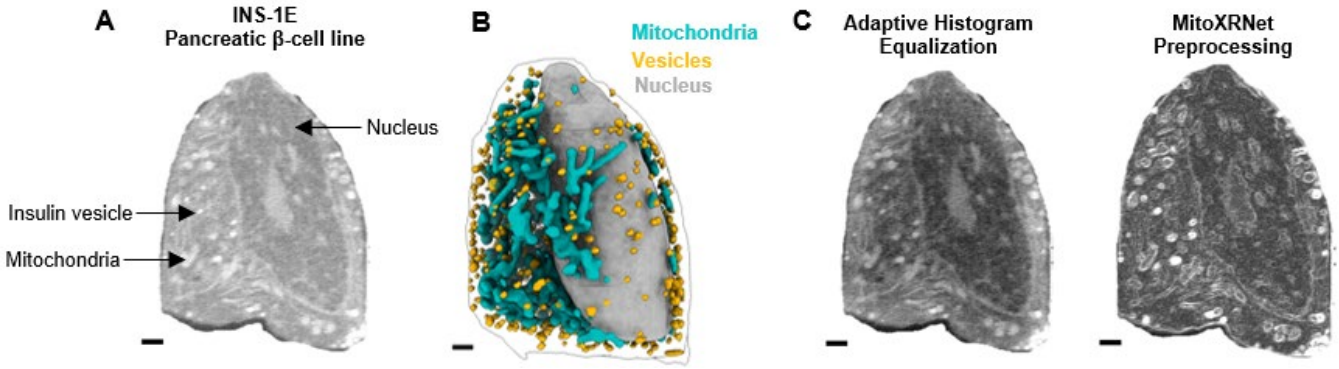

Figure 2: Tomogram preprocessing
(A) 2D slice of a raw tomogram (Image slightly enhanced for visualization).
(B) Manual segmentation of the tomogram in (A).
(C) Adaptive Histogram Equalization (AHE) and Sobel-based high pass filtering with gaussian smoothing and normalization of the slice shown in (A). Scale bars = 1μm

Evaluation of MitoXRNet

We had a total of 55 tomograms from the first dataset, out of which same three tomograms as done by Li et al.[18] were kept in test set. The rest of the tomograms were divided into training (49) and validation (3) sets. Previous work done on segmenting mitochondria and nuclei from SXT tomograms used 2D slices for training the model[18]. Although the 2D slicing approach gave decent quantitative results (Table 1), the qualitative results were very poor as shown in Figure 3. The reason being that 2D slices do not preserve the full volumetric context of organelles and subcellar structures. To provide volumetric context and preserve the spatial continuity of mitochondria morphology we used 3D slices, as described in the previous workflow section.

Initially, we trained a significantly small network (MitoXRNet-s) with only 1.4 million parameters. The model was trained on two different losses separately: one with BCE (Binary Cross Entropy) Loss and another with a combination of robust Dice Loss and BCE Loss. We saw that the addition of robust dice loss provided stability to overall loss by reducing the deviation in DICE score values (Table 1) and is better where class imbalance is extreme. The proposed approach of using 3D slicing along with preprocessing gives better quantitative (Table 1) and qualitative (Figure 3) results.

The nnU-Net was auto-configured to a 31.2 million parameter full-resolution 3D U-Net model that uses 3D blocks, rather than 3D slices. From (Table 1), we can see that the

average Dice score on in-domain test cells is highest for MitoXRNet, outperforming Li et al[18] and nnU-Net[23]. Although MitoXRNet achieved the highest dice score for mitochondria with BCE loss (73.83%), the standard deviation is also high (±5.49%), whereas, with combined loss, even though the average value is slightly reduced (73.59%), the deviation decreases significantly (±1.41%).

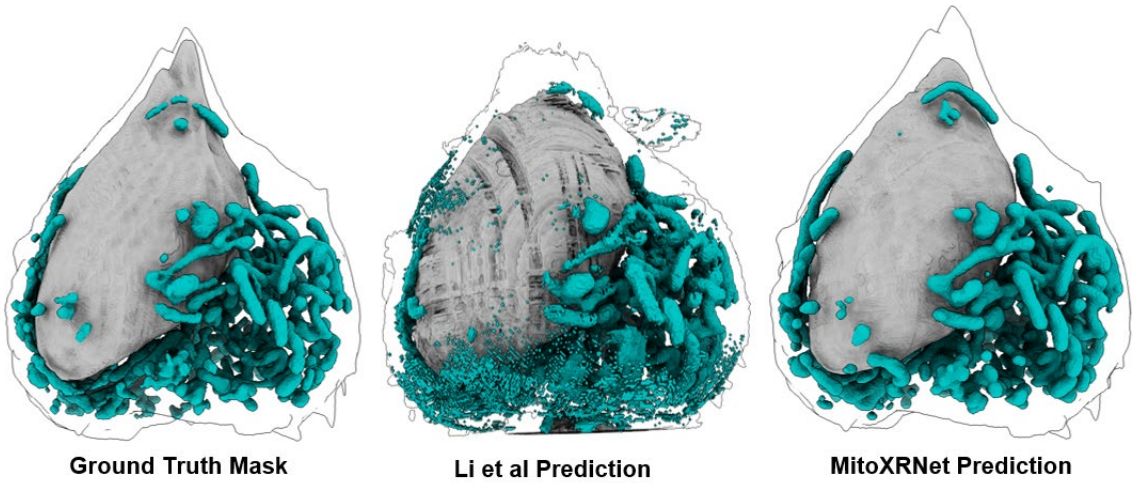

Figure 1: Auto-segmentation comparison: Manual segmentation (Left), Predicted masks of mitochondria and nucleus from Li et al.[18] (Middle) and MitoXRNet (Right).

Table 1. Dice score (in %) on in-domain test set. The table compares the dice scores from Li et al.[18] (recomputed), nnU-Net[23] and MitoXRNet. MitoXRNet was trained with two separate loss functions. The threshold value represents the cut-off value for converting probabilistic masks to binary masks.

Cell ID	Li et al.		nnU-Net		MitoXRNet-s (BCE Loss, threshold = 0.5)		MitoXRNet-s (Combined Loss, threshold = 0.6)	
	Mito	Nucleus	Mito	Nucleus	Mito	Nucleus	Mito	Nucleus
766_8	70.4	93.92	77.65	96.14	77.72	97.20	73.70	94.85
784_5	58.05	92.97	67.16	94.72	77.70	96.44	75.26	95.03
842_17	64.36	89.48	66.06	90.25	66.06	89.99	71.82	89.64
Average	64.27	92.12	73.41	93.70	**73.83**	**94.54**	73.59	93.17
Std	5.04	1.91	4.51	2.51	5.49	3.23	**1.41**	2.50

Comparing manual and auto-segmented masks

To analyze the quality of our predictions and further investigate the reason for still missing on the significant amount of Dice score, we compared MitoXRNet segmentations with the ground truth. Figure 4 shows three example regions from in-domain test set cell (cell ID: 842_17) where the prediction and ground truth did not match. In Figure 4A we can see that the ground truth is overly segmented to the extent that it includes surrounding vesicles as part of mitochondrial network whereas

MitoXRNet successfully segments only the actual mitochondrial volume. In Figure 4B, C we can see the same trend of wrongly segmented vesicles as mitochondria in the ground truth which our model correctly distinguishes and predicts only the true mitochondria. Our analysis shows that the errors on ground truth masks increase false negatives fraction, reducing the overall Dice score.

Evaluation of out-of-domain test set

We also evaluated the performance of MitoXRNet on an independent out-of-domain test dataset with 44 tomograms. The details of this dataset are mentioned in Methods: Dataset. Although the 3D U-Net model with 1.4 million parameters performed well on the in-domain dataset, its generalizability appeared limited when evaluated on out-of-domain data. The initial model with 1.4M parameters only achieved 64.63±10.2% with BCE loss, 60.95±15.33% with combined loss, whereas nnU-Net scored 68.96±16.15% average dice score.

So, we trained a larger variant of MitoXRNet with 22.6 million parameters (MitoXRNet-l), but still smaller than 31.2 million parameters nnU-Net. When increasing the depth of the model, we saw the same level of performance on the in-domain test set (73.16±3.74%) but significantly improved generalization on out-of-domain dataset (69.28±10.74%.). It did not only perform better than nnU-Net on average dice but also improved on the variation (from ±16.15% to ±10.74%).

Discussion

This study presents a robust and efficient methodology for the auto segmentation of mitochondria and nucleus from Soft X-ray tomograms. We demonstrated that appropriate preprocessing can significantly enhance mitochondrial representation in tomograms thus improving the model's ability to recognize structural variations. Furthermore, incorporating volumetric context—by training on overlapping 3D slices along all three axes rather than 2D slices—substantially improved segmentation quality and accuracy. Using Sobel-based preprocessing, MitoXRNet achieved better segmentation compared to both the 2D segmentation approach by Li *et al.*[18]and the self-configuring nnU-Net[23], despite having only 1.4M parameters for in-domain data and 22.6M parameters for out-of-domain datasets.

In one of the in-domain test cells, we identified multiple regions where vesicles were incorrectly labeled as mitochondria in the ground truth. Such mislabeling increases the contribution of false negatives and lowers the Dice score, indicating that the model's actual performance is likely to be better than what is indicated by current dice score value. Additionally, we observed that a few insulin vesicles were occasionally predicted as mitochondria due to their morphological similarity with small mitochondria, leading to increase in false positives.

To address these errors and further improve the segmentation accuracy, future work could explore boundary-aware loss functions and advanced architectures. Moreover, co-predicting multiple organelle masks could improve the segmentation accuracy for each organelle. However, vesicle segmentation remains challenging due to extreme class imbalance relative to mitochondria and nucleus. Addressing this will require adaptation of adequate preprocessing techniques and loss functions.

Overall, MitoXRNet establishes a scalable and accurate framework for 3D segmentation of organelles in Soft X-ray tomograms. This work lays the foundation for systematic studies of cellular architecture and its alterations under various physiological and pathological conditions.

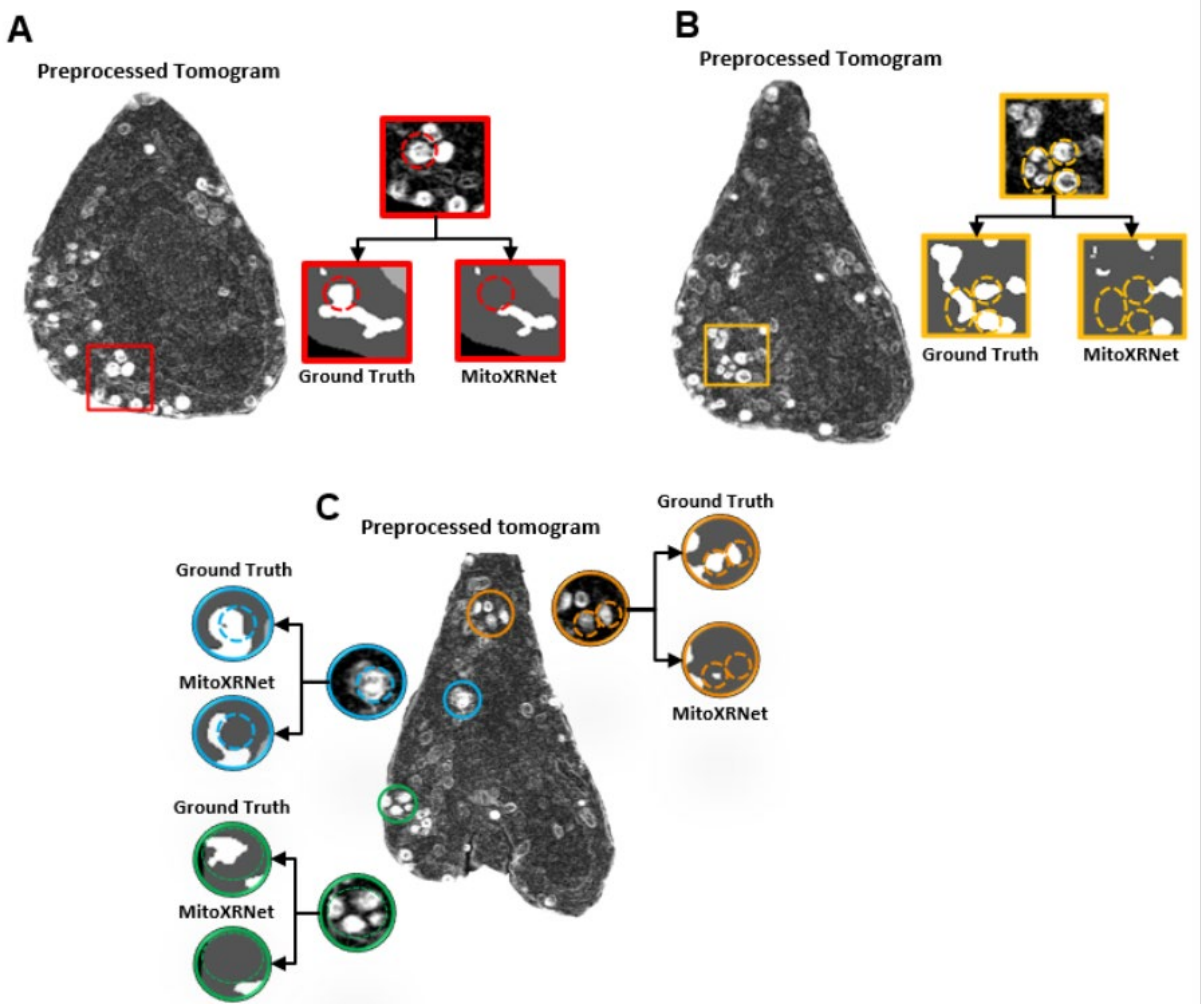

Figure 4: Comparison of predicted and ground-truth masks. (A), (B), (C) Showing three example regions in cell contrast enhanced 842_17 cell, where the ground truth mask of mitochondria includes vesicles, but the predicted mask avoids vesicle region.

Methods

Experimental model and study participant details

Soft-X-ray tomography

Image projections were collected at 517 eV using XM-2[38] soft X-ray microscope at the National Center for X-Ray Tomography at the Advanced Light Source (Lawrence Berkeley National Laboratory); the microscope was equipped with a 50-nm zone plate. During data collection cells were maintained in a stream of helium gas cooled to liquid nitrogen temperature. Projection images were collected sequentially around a rotation axis of 180^o(capillary axis), with 2° increments and an exposure time of 350ms. Tomograms were reconstructed from the acquired projections using AREC3D, with voxel intensity normalized to attribute accurate linear absorption coefficient (LAC) values across all samples.

Dataset

The first dataset was obtained from previous publications by White et al.[35] and Loconte et al.[36], containing a total of 55 tomograms of Rat insulinoma INS-1E cell line from Addex Bio, collected with 60-nm zone plate. The second dataset used for out-of-domain testing was obtained from Deshmukh et al.[37], containing 44 tomograms of Rat insulinoma INS-1E cells from Pierre Maechler's lab (University of Geneva)[39], collected with 50-nm zone plate.

Method Details

Preprocessing of 3D Soft X-Ray tomograms

To enhance mitochondrial structures in the 3D soft X-ray tomograms, we applied a combination of Gaussian smoothing and Sobel-based high-pass filtering. First, the raw image volume I was smoothed with a Gaussian filter G_σ of standard deviation σ=2, generating

$$I' = I + G_\sigma * I$$

where $*$ denotes convolution. Edge information was then extracted using a 3D Sobel operator along the x, y and z directions:

$$S_x = \nabla_x I', \qquad S_y = \nabla_y I', \qquad S_z = \nabla_z I'$$

and the Sobel magnitude was computed as

$$S = \sqrt{S_x^2 + S_y^2 + S_z^2}$$

This high-pass response was combined with the original image in a nonlinear form:

$$I'' = I + 0.75S + 0.25S^2$$

where the quadratic term enhances strong edges while suppressing noise. Finally, both I'' and I were normalized to the range [0,1] and multiplicatively combined to yield the preprocessed tomogram:

$$I_{final} = Norm(I'') \cdot Norm(I)$$

This procedure emphasizes fine mitochondrial boundaries while retaining overall structural contrast, thereby facilitating more accurate segmentation.

Generating Cell, Nucleus and Mitochondria masks

The ground truth cell masks were generated using ACSeg[19]. The cell masks from ACSeg were refined manually by the experimentalist to prevent any error accumulation in the training of mitochondria and nucleus segmentation.. The ground truth masks for mitochondria and nucleus were manually segmented using Amira (FEI) software.

Resizing and 3D Slicing

Soft X-ray tomograms have different dimensions along each axis and between different datasets due to different resolutions and variable field of view. The tomograms after preprocessing and cytoplasm segmentation using ACseg[19], were resized to $704 \times 704 \times 704$ voxels using zero center padding. Further, the tomograms were sliced along the three axes independently, generating 3D slices of size $64 \times 704 \times 704$, with sliding window of 32 voxels. This creates an overlap of 32 voxel depth between two 3D slices. Single tomogram generates 21 3D slices in each direction with total of 63 3D slices.

Model training

For training the model out of 55 tomograms in first dataset, 49 tomograms were used for training, 3 for validation and 3 for testing. Another dataset with 44 tomograms was used for out-of-domain testing. In total we used 3087 training, 189 validation and 189 test slices from the 55 padded tomograms.

In this work, we implemented two configurations of 3D U-Net based on number of layers and filters. One model with 1.4M parameters using 4 encoder-decoder blocks along with Batch Normalization[40], with 1, 8, 16, 32 and 64 (bottleneck Conv layer) kernels in each block respectively. Another model with 22.6M parameters using 5 encoder-decoder blocks and 1, 16, 32, 64, 128 and 256 (bottleneck Conv layer) kernels. Both the models were trained with a batch size of 4 slices using Adam

optimizer[41] with a fixed learning rate of $1e^{-4}$. Both the models were trained under two loss functions independently, corresponding to two separate training regimes.

Loss functions

This study uses two loss functions. The formulation of both loss function over a single 3D-slice is defined below.

1. Binary Cross-Entropy (BCE) Loss

$$L_{BCE} = -\frac{1}{N}\sum_{i=1}^{N}(y_i \log(p_i) + (1 - y_i)\log(1 - p_i))$$

where N is the total number of voxels in the slice, y_i is the true binary label and $p_i = \sigma(z_i)$ is the predicted probability at voxel i computed using sigmoid function.

2. Combined Loss of Robust Dice and BCE Loss

$$L_{RobustDice} = 1 - \frac{2\sum_{i=1}^{N} p_i y_i + \varepsilon}{\sum_{i=1}^{N} p_i^2 + \sum_{i=1}^{N} y_i^2 + \varepsilon}$$

$$L_{CombinedLoss} = \alpha L_{BCE} + (1 - \alpha) L_{RobustDice}$$

where, N, y_i and p_i are as defined above, ε is a small value for numerical stability and α is the hyperparameter for linear combination of BCE and Robust Dice loss. In this study we used $\alpha = 0.5$.

Merge 3D slice predictions

The training of the model occurs at a single 3D slice level, however, to obtain the segmented mask for complete mitochondria and nucleus, predictions from all overlapping 3D slices along the three axes are combined into a single mask.

For each slice s, the model outputs logits for two classes (i.e. nucleus and mitochondria). Let $z_s^{(c)}(u)$ be the logit predicted for class $c \in \{nucleus, mitochondria\}$ at local coordinate u in slice s. These logits are converted to probabilities independently for each class using the sigmoid functions:

$$p_s^{(c)}(u) = \frac{1}{1 + \exp\left(-z_s^{(c)}(u)\right)}$$

Once probabilities are computed from all 63 3D-slices (21 along each axis), they are mapped back to the global 3D volume of the cell. Because the same voxel is predicted multiple times (due to slice overlaps and predictions from all three axes), voxel-wise probabilities are averaged across all occurrences for each class independently. This generates two probabilistic masks, one for each class. Next, class-wise probabilistic masks are merged into a single two-class probabilistic mask by assigning each voxel to the class with higher probability. Finally, to obtain binary segmentation masks, a

threshold is applied. Voxels with probability below the threshold are classified as background, while remaining voxels are assigned to either nucleus or mitochondria based on higher probability.

Acknowledgments

The work was funded by Chellaram Diabetes Research Centre (CDRC). We also thank IIT Roorkee for providing additional financial support for computing resources. We thank Valentina Loconte for her contribution to the data collection efforts. We thank Riva for the help in designing figures.

Author contributions

Conceptualization, J.S.; Data curation, A.D. and K.L.W.; Formal analysis, A.Y.; Funding acquisition, J.S.; Methodology, A.Y., P.B., A.B.; Writing-original draft, A.Y.; Writing-review & editing, A.D, J.S., K.L.W.

Declaration of interests

The authors declare no competing interests.

References

1. Loconte, V., Chen, J.H., Cortese, M., Ekman, A., Le Gros, M.A., Larabell, C., Bartenschlager, R., and Weinhardt, V. (2021). Using soft X-ray tomography for rapid whole-cell quantitative imaging of SARS-CoV-2-infected cells. Cell Reports Methods *1*. https://doi.org/10.1016/j.crmeth.2021.100117.
2. McDermott, G., Le Gros, M.A., Knoechel, C.G., Uchida, M., and Larabell, C.A. (2009). Soft X-ray Tomography and Cryogenic Light Microscopy: The Cool Combination in Cellular Imaging. Trends Cell Biol *19*, 587. https://doi.org/10.1016/J.TCB.2009.08.005.
3. Parkinson, D.Y., McDermott, G., Etkin, L.D., Le Gros, M.A., and Larabell, C.A. (2008). Quantitative 3-D imaging of eukaryotic cells using soft x-ray tomography. J Struct Biol *162*, 380. https://doi.org/10.1016/J.JSB.2008.02.003.
4. White, K.L., Singla, J., Loconte, V., Chen, J.-H., Ekman, A., Sun, L., Zhang, X., Francis, J.P., Li, A., Lin, W., et al. (2020). Visualizing subcellular rearrangements in intact β cells using soft x-ray tomography.
5. Loconte, V., Singla, J., Li, A., Chen, J.H., Ekman, A., McDermott, G., Sali, A., Le Gros, M., White, K.L., and Larabell, C.A. (2022). Soft X-ray tomography to map and quantify organelle interactions at the mesoscale. Structure *30*, 510-521.e3. https://doi.org/10.1016/j.str.2022.01.006.
6. Elgass, K.D., Smith, E.A., LeGros, M.A., Larabell, C.A., and Ryan, M.T. (2015). Analysis of ER-mitochondria contacts using correlative fluorescence microscopy and soft X-ray tomography of mammalian cells. J Cell Sci *128*, 2795–2804.

https://doi.org/10.1242/JCS.169136/260390/AM/ANALYSIS-OF-ER-MITOCHONDRIA-CONTACTS-BY.

7. Padovani, F., Mairhörmann, B., Falter-Braun, P., Lengefeld, J., and Schmoller, K.M. (2022). Segmentation, tracking and cell cycle analysis of live-cell imaging data with Cell-ACDC. BMC Biol *20*, 1–18. https://doi.org/10.1186/S12915-022-01372-6/TABLES/4.
8. Stringer, C., Wang, T., Michaelos, M., and Pachitariu, M. (2021). Cellpose: a generalist algorithm for cellular segmentation. Nat Methods *18*, 100–106. https://doi.org/10.1038/S41592-020-01018-X;SUBJMETA.
9. Zargari, A., Topacio, B.R., Mashhadi, N., and Shariati, S.A. (2024). Enhanced cell segmentation with limited training datasets using cycle generative adversarial networks. iScience *27*, 109740. https://doi.org/10.1016/j.isci.2024.109740.
10. Fischer, C.A., Besora-Casals, L., Rolland, S.G., Haeussler, S., Singh, K., Duchen, M., Conradt, B., and Marr, C. (2020). MitoSegNet: Easy-to-use Deep Learning Segmentation for Analyzing Mitochondrial Morphology. iScience *23*. https://doi.org/10.1016/j.isci.2020.101601.
11. Ounkomol, C., Seshamani, S., Maleckar, M.M., Collman, F., and Johnson, G.R. (2018). Label-free prediction of three-dimensional fluorescence images from transmitted-light microscopy. Nat Methods *15*, 917–920. https://doi.org/10.1038/S41592-018-0111-2;SUBJMETA.
12. Conrad, R., and Narayan, K. (2022). Instance segmentation of mitochondria in electron microscopy images with a generalist deep learning model. bioRxiv, 2022.03.17.484806. https://doi.org/10.1101/2022.03.17.484806.
13. Taşel, F.S., and Çiftci, E. (2025). MitoSeg: Mitochondria segmentation tool. SoftwareX *30*, 102081. https://doi.org/10.1016/J.SOFTX.2025.102081.
14. Jang, C., Lee, H., Yoo, J., and Yoon, H. (2025). Deep learning-driven automated mitochondrial segmentation for analysis of complex transmission electron microscopy images. Sci Rep *15*, 1–13. https://doi.org/10.1038/S41598-025-03311-1;SUBJMETA.
15. Shi, R., Duan, L., Huang, T., and Jiang, T. (2024). Evidential Uncertainty-Guided Mitochondria Segmentation for 3D EM Images. Proceedings of the AAAI Conference on Artificial Intelligence *38*, 4847–4855. https://doi.org/10.1609/AAAI.V38I5.28287.
16. Heinrich, L., Bennett, D., Ackerman, D., Park, W., Bogovic, J., Eckstein, N., Petruncio, A., Clements, J., Pang, S., Xu, C.S., et al. (2021). Whole-cell organelle segmentation in volume electron microscopy. Nature *599*, 141–146. https://doi.org/10.1038/S41586-021-03977-3;TECHMETA.
17. Francis, J.P., Wang, H., White, K., Syeda-Mahmood, T., and Stevens, R. (2020). Neural Network Segmentation of Cell Ultrastructure Using Incomplete Annotation. Proceedings - International Symposium on Biomedical Imaging *2020-April*, 1183–1187. https://doi.org/10.1109/ISBI45749.2020.9098739.
18. Li, A., Zhang, X., Singla, J., White, K., Loconte, V., Hu, C., Zhang, C., Li, S., Li, W., Francis, J.P., et al. (2022). Auto-segmentation and time-dependent

systematic analysis of mesoscale cellular structure in β-cells during insulin secretion. PLoS One *17*, e0265567. https://doi.org/10.1371/JOURNAL.PONE.0265567.

19. Erozan, A., Lösel, P.D., Heuveline, V., and Weinhardt, V. (2024). Automated 3D cytoplasm segmentation in soft X-ray tomography. iScience *27*. https://doi.org/10.1016/J.ISCI.2024.109856/ASSET/905733F2-DB75-43EC-922E-76BE2CEDED8D/MAIN.ASSETS/GR6.JPG.
20. Erozan, A., Zeilmann, A., Chatzimpinou, A., Annesha, F.M., Heuveline, V., and Weinhardt, V. (2025). Spatially-Informed Multi-Stage Active Learning for Segmentation of Nucleus in Soft X-ray Tomography. 2025 IEEE Symposium on Computational Intelligence in Image, Signal Processing and Synthetic Media, CISM 2025. https://doi.org/10.1109/CISM64958.2025.11060865.
21. Chueh, S., Brink, M.C., Simpson, J.C., and Kapishnikov, S. (2025). SXTractor: A Self-Supervised Feature Extractor of Soft X-Ray Images That Enables Few-Shot Tomogram Segmentation. bioRxiv, 2025.08.25.672073. https://doi.org/10.1101/2025.08.25.672073.
22. Chen, J., Mirvis, M., Ekman, A., Vanslembrouck, B., Gros, M. Le, Larabell, C., and Marshall, W.F. (2024). Automated segmentation of soft X-ray tomography: native cellular structure with sub-micron resolution at high throughput for whole-cell quantitative imaging in yeast. bioRxiv, 2024.10.31.621371. https://doi.org/10.1101/2024.10.31.621371.
23. Isensee, F., Jaeger, P.F., Kohl, S.A.A., Petersen, J., and Maier-Hein, K.H. (2021). nnU-Net: a self-configuring method for deep learning-based biomedical image segmentation. Nat Methods *18*, 203–211. https://doi.org/10.1038/S41592-020-01008-Z;SUBJMETA=114,1564,308,575,631,692;KWRD=IMAGE+PROCESSING,TRANSLATIONAL+RESEARCH.
24. Francis, J.P., Wang, H., White, K., Syeda-Mahmood, T., and Stevens, R. (2020). Neural Network Segmentation of Cell Ultrastructure Using Incomplete Annotation. Proceedings - International Symposium on Biomedical Imaging *2020-April*, 1183–1187. https://doi.org/10.1109/ISBI45749.2020.9098739.
25. Harkiolaki, M., Darrow, M.C., Spink, M.C., Kosior, E., Dent, K., and Duke, E. (2018). Cryo-soft X-ray tomography: using soft X-rays to explore the ultrastructure of whole cells. Emerg Top Life Sci *2*, 81. https://doi.org/10.1042/ETLS20170086.
26. Singla, J., and White, K.L. (2021). A community approach to whole-cell modeling. Curr Opin Syst Biol *26*, 33–38. https://doi.org/10.1016/J.COISB.2021.03.009.
27. Singla, J., McClary, K.M., White, K.L., Alber, F., Sali, A., and Stevens, R.C. (2018). Opportunities and Challenges in Building a Spatiotemporal Multi-scale Model of the Human Pancreatic β Cell. Cell *173*, 11–19. https://doi.org/10.1016/j.cell.2018.03.014.
28. Loconte, V., Chen, J.-H., Vanslembrouck, B., Ekman, A.A., McDermott, G., Gros, M.A. Le, and Larabell, C.A. (2023). The Role of Soft X-ray Tomography in

Generating Whole-cell Models. Microscopy and Microanalysis *29*, 1170–1170. https://doi.org/10.1093/MICMIC/OZAD067.600.

29. Loconte, V., Singla, J., Li, A., Chen, J.-H., Ekman, A., McDermott, G., Sali, A., Gros, M. Le, White, K.L., and Larabell, C.A. (2023). Soft X-ray Tomography for Mapping and Quantifying Intracellular Organelle Interactions. Microscopy and Microanalysis *29*, 1181–1181. https://doi.org/10.1093/MICMIC/OZAD067.607.
30. Chethan, K.S., Sinchana, G.S., Nataraj, K.R., and Choodarathnakara, A.L. (2019). Analysis of Image Quality using Sobel Filter. Proceedings of the 3rd International Conference on Inventive Systems and Control, ICISC 2019, 526–531. https://doi.org/10.1109/ICISC44355.2019.9036369.
31. Zhang, J.Y., Yan, C., and Huang, X.X. (2009). Edge detection of images based on improved sobel operator and genetic algorithms. Proceedings of 2009 International Conference on Image Analysis and Signal Processing, IASP 2009, 32–35. https://doi.org/10.1109/IASP.2009.5054605.
32. Ganesan, P., and Sajiv, G. (2017). A comprehensive study of edge detection for image processing applications. Proceedings of 2017 International Conference on Innovations in Information, Embedded and Communication Systems, ICIIECS 2017 *2018-January*, 1–6. https://doi.org/10.1109/ICIIECS.2017.8275968.
33. Jia, D., Xiao, C.L., and Sun, J.G. (2015). Edge detection method of Gaussian block distance. Proceedings - International Conference on Image Processing, ICIP *2015-December*, 3049–3053. https://doi.org/10.1109/ICIP.2015.7351363.
34. Kremer, J.R., Mastronarde, D.N., and McIntosh, J.R. (1996). Computer visualization of three-dimensional image data using IMOD. J Struct Biol *116*, 71–76. https://doi.org/10.1006/jsbi.1996.0013.
35. White, K.L., Singla, J., Loconte, V., Chen, J.H., Ekman, A., Sun, L., Zhang, X., Francis, J.P., Li, A., Lin, W., et al. (2020). Visualizing subcellular rearrangements in intact β cells using soft x-ray tomography. Sci Adv *6*. https://doi.org/10.1126/SCIADV.ABC8262.
36. Loconte, V., Singla, J., Li, A., Chen, J.H., Ekman, A., McDermott, G., Sali, A., Le Gros, M., White, K.L., and Larabell, C.A. (2022). Soft X-ray tomography to map and quantify organelle interactions at the mesoscale. Structure *30*, 510-521.e3. https://doi.org/10.1016/j.str.2022.01.006.
37. Deshmukh, A., Chang, K., Cuala, J., Campos, M.J.H., Mahmood, S., Verma, R., Georgia, S., Loconte, V., and White, K.L. (2025). Secretory stimuli distinctly regulate insulin secretory granule maturation through structural remodeling. bioRxiv, 2025.03.29.644646. https://doi.org/10.1101/2025.03.29.644646.
38. Le Gros, M.A., Mcdermott, G., Cinquin, B.P., Smith, E.A., Do, M., Chao, W.L., Naulleau, P.P., and Larabell, C.A. (2014). Biological soft X-ray tomography on beamline 2.1 at the Advanced Light Source. J Synchrotron Radiat *21*, 1370–1377. https://doi.org/10.1107/S1600577514015033.
39. Merglen, A., Theander, S., Rubi, B., Chaffard, G., Wollheim, C.B., and Maechler, P. (2004). Glucose Sensitivity and Metabolism-Secretion Coupling Studied

during Two-Year Continuous Culture in INS-1E Insulinoma Cells. Endocrinology *145*, 667–678. https://doi.org/10.1210/EN.2003-1099.

40. Ioffe, S., and Szegedy, C. (2015). Batch Normalization: Accelerating Deep Network Training by Reducing Internal Covariate Shift. Preprint at PMLR.
41. Kingma, D.P., and Ba, J.L. (2014). Adam: A Method for Stochastic Optimization. 3rd International Conference on Learning Representations, ICLR 2015 - Conference Track Proceedings.